

The following resources related to this article are available online at www.sciencemag.org (this information is current as of January 1, 2010):

Updated information and services, including high-resolution figures, can be found in the online version of this article at:

<http://www.sciencemag.org/cgi/content/full/317/5841/1079>

Supporting Online Material can be found at:

<http://www.sciencemag.org/cgi/content/full/317/5841/1079/DC1>

A list of selected additional articles on the Science Web sites **related to this article** can be found at:

<http://www.sciencemag.org/cgi/content/full/317/5841/1079#related-content>

This article **cites 22 articles**, 7 of which can be accessed for free:

<http://www.sciencemag.org/cgi/content/full/317/5841/1079#otherarticles>

This article has been **cited by** 39 article(s) on the ISI Web of Science.

This article has been **cited by** 10 articles hosted by HighWire Press; see:

<http://www.sciencemag.org/cgi/content/full/317/5841/1079#otherarticles>

This article appears in the following **subject collections**:

Neuroscience

<http://www.sciencemag.org/cgi/collection/neuroscience>

Information about obtaining **reprints** of this article or about obtaining **permission to reproduce this article** in whole or in part can be found at:

<http://www.sciencemag.org/about/permissions.dtl>

When assayed individually, the mutant enzymes Lys¹¹¹⁹→Gln¹¹¹⁹ (K1119Q) and K718Q exhibited 0.1 and 4% wild-type activity, respectively (table S4). Hybrid tetramers were created by mixing and diluting the mutants together before assaying for enzyme activity. Dilution of PC promotes equilibration among monomers, dimers, and tetramers (23) and allows a mixed heterotetramer population to reassociate. The mixed population of heterotetramers exhibited 20% wild-type activity (table S3), nearly five times as much as that observed with either mutant homotetramer and near to the maximum predicted activity of 26% (fig. S4). The recovery of activity on reassociation is possible only if the hybrid tetramers recombine to restore a functional pair of neighboring active sites, capable of transferring the tethered carboxybiotin intermediate between two opposing chains. The transfer of a carboxybiotin intermediate between active sites on separate polypeptide chains is a previously unrecognized feature of PC catalysis. Several multifunctional enzymes have similarly been shown to transfer their tethered intermediates between active sites on opposing polypeptide chains (24, 25), suggesting that intermolecular intermediate transfer is a common and essential feature of catalysis.

Ethyl-CoA is bound to only one monomer of the RePC asymmetric dimer, permitting a direct comparison of the consequences of activator binding on domain arrangement and orientation. A superposition of the two monomers reveals a 40° rotation and a translocation of nearly 40 Å in the BC active site, centered at the ethyl-CoA binding site of the allosteric domain (Fig. 4). In the tetramer, ethyl-CoA is bound to both monomers on the top face, and the BC active site is positioned ~65 Å from its opposing CT active-site pair (Fig. 3B). On the bottom face of the tetramer, ethyl-CoA is unbound, and the distance between the opposing active-site pairs increases to ~80 Å (Fig. 3C). The rotation in the BC domain inhibits acetyl-CoA binding on the bottom face of the tetramer. Thus, only two binding sites are available per tetramer, which is consistent with the Hill coefficient observed for yeast PC (26) and with the observation that only 50% of acetyl-CoA binding sites are occupied in yeast PC (27). The structure suggests that acetyl-CoA activates PC by decreasing the distance between neighboring active sites. While the active-site pairs on the top face of the tetramer are pushed closer together, the active-site pairs on the bottom face are pulled farther apart. This is a rare example of allosteric activation paired with negative cooperativity and implies that half of the active-site pairs are more active than the others. Recent kinetic studies and numerical simulations support half-sites reactivity for the BC subunit of ACC (28), suggesting that this mechanism is conserved among enzymes of the biotin-dependent family. Such half-sites reactivity may permit PC to affect efficient catalysis while maintaining its *in vivo* association with other metabolic enzymes (29).

The allosteric binding site in PC offers a target for modifiers of activity that may be useful

in the treatment of obesity or type 2 diabetes, and the mechanistic insights gained from the complete structural description of RePC permit detailed investigations into the individual catalytic and regulatory sites of the enzyme. Furthermore, as a consequence of its fully defined domain architecture, PC represents a paradigm for understanding interdomain arrangement and allosteric regulation in multifunctional enzymes.

References and Notes

1. F. M. Raushel, J. B. Thoden, H. M. Holden, *Acc. Chem. Res.* **36**, 539 (2003).
2. R. N. Perham, *Annu. Rev. Biochem.* **69**, 961 (2000).
3. S. Jitrapakdee, J. C. Wallace, *Curr. Protein Pept. Sci.* **4**, 217 (2003).
4. L. Tong, *Cell. Mol. Life Sci.* **62**, 1784 (2005).
5. S. Jitrapakdee, A. Vidal-Puig, J. C. Wallace, *Cell. Mol. Life Sci.* **63**, 843 (2006).
6. S. Kondo *et al.*, *Acta Crystallogr. D* **60**, 486 (2004).
7. P. R. Hall *et al.*, *EMBO J.* **23**, 3621 (2004).
8. E. L. Roberts *et al.*, *Biochemistry* **38**, 5045 (1999).
9. R. Studer *et al.*, *J. Mol. Biol.* **367**, 547 (2007).
10. P. V. Attwood, J. C. Wallace, *Acc. Chem. Res.* **35**, 113 (2002).
11. Materials and methods are available as supporting material on Science Online.
12. M. Y. Galperin, E. V. Koonin, *Protein Sci.* **6**, 2639 (1997).
13. J. B. Thoden, C. Z. Blanchard, H. M. Holden, G. L. Waldrop, *J. Biol. Chem.* **275**, 16183 (2000).
14. J. B. Thoden, G. Wesenberg, F. M. Raushel, H. M. Holden, *Biochemistry* **38**, 2347 (1999).
15. J. B. Thoden, S. Firestine, A. Nixon, S. J. Benkovic, H. M. Holden, *Biochemistry* **39**, 8791 (2000).
16. J. Yong-Biao, M. N. Islam, S. Sueda, H. Kondo, *Biochemistry* **43**, 5912 (2004).
17. S. Jitrapakdee, J. C. Wallace, *Biochem. J.* **340**, 1 (1999).
18. F. Dydá, D. C. Klein, A. B. Hickman, *Annu. Rev. Biophys. Biomol. Struct.* **29**, 81 (2000).
19. E. Krissinel, K. Henrick, *Acta Crystallogr. D* **60**, 2256 (2004).
20. P. G. Peters-Wendisch, V. F. Wendisch, S. Paul, B. J. Eikmanns, H. Sahm, *Microbiology* **143**, 1095 (1997).
21. D. V. Reddy, S. Rothmund, B. C. Shenoy, P. R. Carey, F. D. Sonnichsen, *Protein Sci.* **7**, 2156 (1998).
22. R. N. Perham, *Biochemistry* **30**, 8501 (1991).
23. P. V. Attwood, W. Johannssen, A. Chapman-Smith, J. C. Wallace, *Biochem. J.* **290**, 583 (1993).
24. V. S. Rangan, A. K. Joshi, S. Smith, *J. Biol. Chem.* **273**, 34949 (1998).
25. Y. Tang, C. Y. Kim, I. I. Mathews, D. E. Cane, C. Khosla, *Proc. Natl. Acad. Sci. U.S.A.* **103**, 11124 (2006).
26. J. J. Cazzulo, A. O. Stoppani, *Arch. Biochem. Biophys.* **127**, 563 (1968).
27. A. Chapman-Smith, G. W. Booker, P. R. Clements, J. C. Wallace, D. B. Keech, *Biochem. J.* **276**, 759 (1991).
28. M. S. de Queiroz, G. L. Waldrop, *J. Theor. Biol.* **246**, 167 (2007).
29. L. A. Fahien, J. W. Davis, J. Laboy, *J. Biol. Chem.* **268**, 17935 (1993).
30. Y. Kazuta, E. Tokunaga, E. Aramaki, H. Kondo, *FEBS Lett.* **427**, 377 (1998).
31. This work was supported by grants to W.W.C., J.C.W., and P.V.A. from NIH (GM070455) and to I.R. from NIH (AR35186). M.St.M. was supported in part by a fellowship from the Natural Science and Engineering Research Council of Canada. Use of the Structural Biology BM19 beamline Argonne National Laboratory Advanced Photon Source was supported by the U.S. Department of Energy, Office of Energy Research, under contract number W-31-109-ENG-38. We thank M. Dunn for providing the *R. etli* PC clone; V. Klenchin for helpful discussions and critical reading of the manuscript; J. B. Thoden and H. M. Holden for preliminary crystallography trials; A. Netting (Adelaide Microscopy) for technical assistance with metal-ion analysis; and A. Steinberg for his assistance in generating the illustrations. Coordinates and structure factors have been deposited in the Protein Data Bank (www.rcsb.org) with the accession number 2QF7.

Supporting Online Material

www.sciencemag.org/cgi/content/full/317/5841/1076/DC1
Materials and Methods
SOM Text
Figs. S1 to S4
Tables S1 to S4
References

1 May 2007; accepted 5 July 2007
10.1126/science.11444504

When Fear Is Near: Threat Imminence Elicits Prefrontal- Periaqueductal Gray Shifts in Humans

Dean Mobbs,* Predrag Petrovic, Jennifer L. Marchant, Demis Hassabis, Nikolaus Weiskopf, Ben Seymour, Raymond J. Dolan, Christopher D. Frith

Humans, like other animals, alter their behavior depending on whether a threat is close or distant. We investigated spatial imminence of threat by developing an active avoidance paradigm in which volunteers were pursued through a maze by a virtual predator endowed with an ability to chase, capture, and inflict pain. Using functional magnetic resonance imaging, we found that as the virtual predator grew closer, brain activity shifted from the ventromedial prefrontal cortex to the periaqueductal gray. This shift showed maximal expression when a high degree of pain was anticipated. Moreover, imminence-driven periaqueductal gray activity correlated with increased subjective degree of dread and decreased confidence of escape. Our findings cast light on the neural dynamics of threat anticipation and have implications for the neurobiology of human anxiety-related disorders.

Critical to an organism's survival is the ability to switch flexibly between defensive states in response to threat. Within behavioral ecology, a key component of de-

fensive switching is the "predatory imminence continuum" where distinct threat states are configured according to whether a predator is distal or proximal to the prey (1–5). This continuum

encompasses three core stages: “pre-encounter,” where there is risk in the absence of immediate danger; “post-encounter,” where the threat is detected; and “circa-strike,” defined as distal or proximal interaction with the threat stimulus (2).

These stages, relating to the distance from a threat, are associated with distinct patterns of activity at the neurobiological level (6–8). For example, distal threat elicits activity in the prefrontal cortices, which possibly reflects the complex planning of avoidance strategies. As threat becomes proximal, midbrain structures such as the periaqueductal gray (PAG) dominate (3, 6). This shift to phylogenetically older midbrain regions has adaptive value because these

structures control fast reflexive behaviors (e.g., fight, flight, or freeze) as well as fear-induced analgesia. The parallel neural dynamics of threat in humans have yet to be identified.

We hypothesized that brain activity associated with threat detection and distal and proximal distance to threat in humans would mirror those derived from defense systems models developed in rodents. We tested a prediction that detection of distal threat would elicit activity in brain regions associated with value-based and complex decision making, such as the anterior cingulate and ventromedial prefrontal cortex (vmPFC), whereas proximal threat would engage low-level midbrain regions implicated in reflexive escape behavior (i.e., PAG). To test this model, we used high-resolution functional magnetic resonance imaging (fMRI) to examine brain activity in 14 healthy subjects while they performed an active “escape-pain” task within a two-dimensional maze. The paradigm involved the subject trying

to avoid a “virtual predator” that had the capacity to chase, capture, and cause pain of high (three shocks: $AI_{high}^{predator}$) or low (one shock: $AI_{low}^{predator}$) intensity (Fig. 1).

Avoidance time in the maze was significantly longer for $AI_{high}^{predator}$ (mean \pm SD: 24.2 ± 1.6 s) relative to $AI_{low}^{predator}$ (19.4 ± 2.0 s) on escaped conditions ($t_{13} = -9.59$, $P < 0.0005$), suggesting that players were more motivated to escape the $AI_{high}^{predator}$. Speed, defined as number of squares per second, was significantly different between the first half and second half of the conditions ($AI_{high}^{predator}$ $t_{13} = -5.86$, $P < 0.0005$; $AI_{low}^{predator}$ $t_{13} = -5.984$, $P < 0.0005$). However, no significant difference was found for speed between the proximal $AI_{high}^{predator}$ and $AI_{low}^{predator}$ ($t_{13} = -2.94$, $P < 0.773$) conditions. A trend toward significance was evident for the number of times the subjects were captured in the $AI_{high}^{predator}$ ($62.5 \pm 15.9\%$) versus the $AI_{low}^{predator}$ condition ($67.0 \pm 16.4\%$; $t_{13} = -1.5$, $P < 0.14$). Together these results sug-

Wellcome Trust Centre for Neuroimaging, Functional Imaging Laboratory, University College London, London WC1N 3BG, UK.

*To whom correspondence should be addressed. E-mail: d.mobbs@fil.ion.ucl.ac.uk

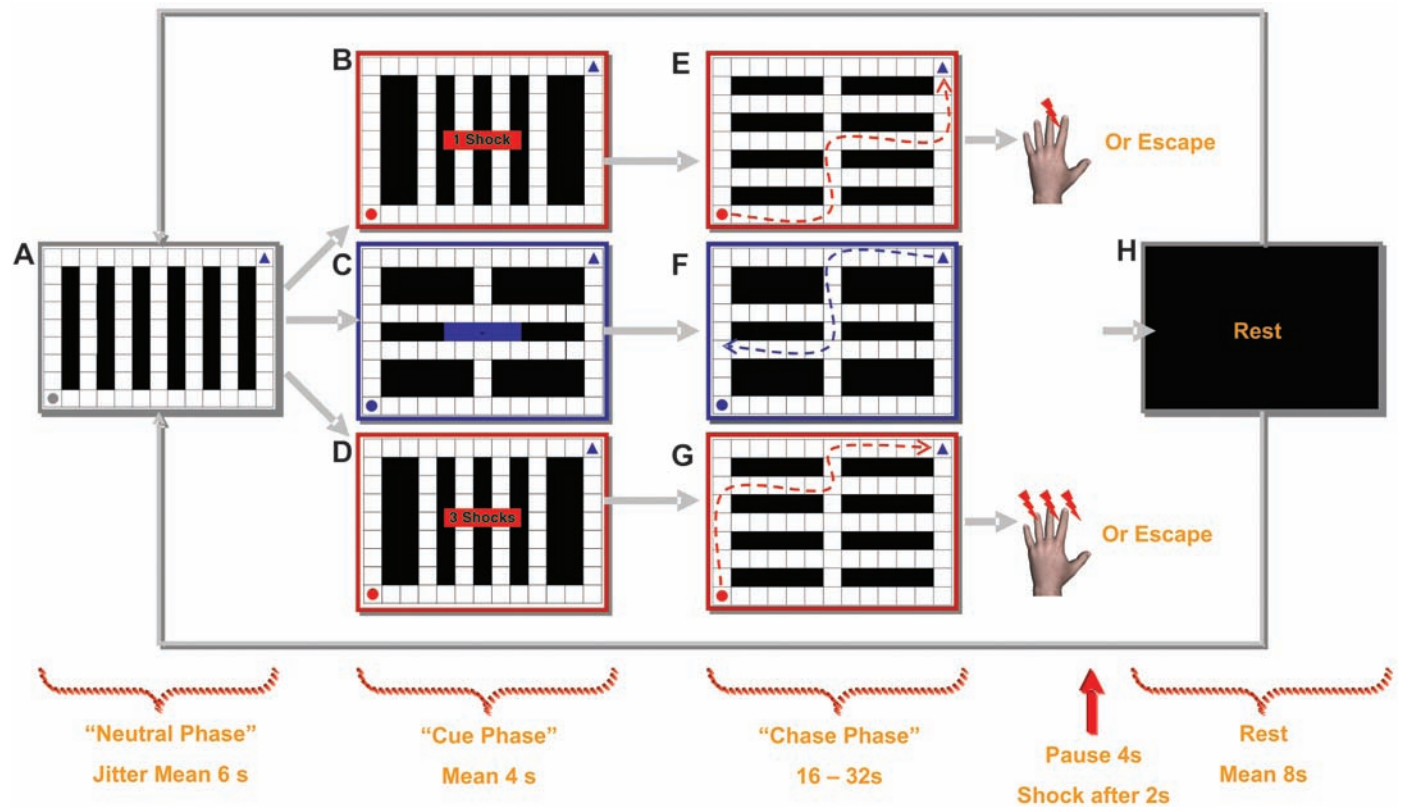


Fig. 1. The virtual predator and prey paradigm. Subjects were presented with a two-dimensional maze containing a 9×13 rectangle grid of walls (black squares) and paths (white squares). All experimental conditions commenced with a “neutral phase” where a preprogrammed artificially intelligent (AI) gray circle ($AI_{neutral}$) appeared at the left-bottom side of the maze (A). The $AI_{neutral}$ was presented on average for 6 s (jitter \pm 2 s) and programmed to wander the maze indiscriminately. After this, the “cue phase” commenced with the $AI_{neutral}$ changed into a predator ($AI_{predator}$) or a yoked control condition. The change from $AI_{neutral}$ to $AI_{predator}$ was signaled by the circle flashing between red and gray. The flashing $AI_{predator}$ appeared for 2 s, and during this time it wandered the maze indiscriminately. Directly after this, subjects were also informed for 2 s of the amount of cutaneous electrical shock they would receive if the $AI_{predator}$ captured them: (B) one shock ($AI_{low}^{predator}$), (C) no shock, or (D) three shocks ($AI_{high}^{predator}$). During the

cue phase, subjects were passive and unable to move the blue triangle situated in the upper right corner of the maze. The “chase phase” began with the $AI_{predator}$ ceasing to flash and the subject moving the blue triangle to (E) escape the $AI_{low}^{predator}$, (F) mimic the movements of the triangle in a replay of a previous experimental condition, or (G) escape the $AI_{high}^{predator}$. (H) After escape or capture, a rest period was presented before the onset of the next trial. To ensure that subjects would not anticipate the end of the chase, we randomly varied the time each $AI_{predator}$ encounter was played (e.g., 16, 20, 24, 28, 32 s). The subjects were not informed that the length of trials varied or given any indication of how much time they had on each trial. To enhance the feelings of spatial distance, mazes were intentionally designed so that chases were long unimpeded runs with no dead-ends. Each block was interleaved with 8, 10, or 12 s of black screen. Further details can be found in the supporting online material.

gest that subjects were more efficient in movement planning and execution when escaping the $AI_{high}^{predator}$.

For the analysis of brain activity, we first examined the evoked blood oxygenation level-dependent (BOLD) responses to the 2-s cue that indicated participants would encounter the $AI_{predator}$ (Fig. 1A and table S1) as compared to the yoked control cue (Fig. 1C). We found enhanced activity in the rostral anterior cingulate cortex [rACC; MNI space coordinates (x, y, z): -6, 41, 22; $Z = 3.85$; $P < 0.0005$] and medial orbitofrontal cortex (mObfc; 6, 49, -19; $Z = 3.42$; $P < 0.0005$), ventral anterior cingulate cortex (vACC; 13, 32, -14; $Z = 4.56$; $P < 0.0005$ uncorrected), and the vmPFC (-4, 39, -13; $Z = 3.48$; $P < 0.0005$).

For the “chase phase,” we first collapsed activity across all $AI_{predator}$ blocks (i.e., $AI_{high}^{predator}$ and $AI_{low}^{predator}$ conditions) and compared them to the yoked blocks. For the $AI_{predator}$ condition, we found increased activity that peaked in the cerebellum (-5, -63, -13; $Z = 5.48$) but extended across the entire PAG (right: 3, -25, -7; $Z = 4.87$; left: -2, -28, -8; $Z = 4.94$) and posterior thalamus including the pulvinar (3, -22, 11; $Z = 4.63$) (Fig. 2B). A different pattern was observed for the yoked minus the $AI_{predator}$ blocks, where activity peaked in the medial PFC (mPFC) (-5, 48, 17; $Z = 5.50$), extending to the right vmPFC (3, 37, -9; $Z = 4.63$) and amygdala (22, -2, -18; $Z = 4.94$) (Fig. 2C and table S2).

We next asked whether there was a relationship between distal and proximal threat and brain activity for the “chase phase” of $AI_{predator}$ (Fig. 3 and table S3). We used a parametric regression between predator distance and BOLD signal, excluding the period in which the shock was administered. Thus, these effects were independent of whether shocks were actually received. Distal threat

was associated with increased activity in the vmPFC, including the subgenual ACC, for both $AI_{high}^{predator}$ (-8, 35, -13; $Z = 3.66$; Fig. 3A) and $AI_{low}^{predator}$ (-10, 38, -11; $Z = 3.93$; Fig. 3B) conditions. Proximal threat was associated with increased activity in the PAG for both $AI_{high}^{predator}$ (left: -3, -33, -15; $Z = 3.58$; right: 8, -32, -21; $Z = 3.73$; Fig. 3C) and $AI_{low}^{predator}$ (6, -33, -14; $Z = 3.02$; fig. S2) conditions. Proximal $AI_{high}^{predator}$ condition also elicited activity in the right dorsal amygdala corresponding with the central nucleus (CeA)/bed nucleus of the stria terminalis (BNST) (32, 4, -13; $Z = 4.78$), whereas the distal $AI_{high}^{predator}$ elicited activity in the right lateral amygdala corresponding to the basolateral amygdala (BLA; 32, -4, -24; $Z = 3.77$). Direct subtraction showed that the $AI_{high}^{predator}$ activated the PAG to a greater extent than did the $AI_{low}^{predator}$ condition (-3, -32, -15; $Z = 3.33$). Conversely, the $AI_{low}^{predator}$ activated the anterior vmPFC (-1, 51, -1; $Z = 3.81$) and BLA (31, -4, -23; $Z = 4.09$) to a greater extent than did the $AI_{high}^{predator}$ condition (fig. S4).

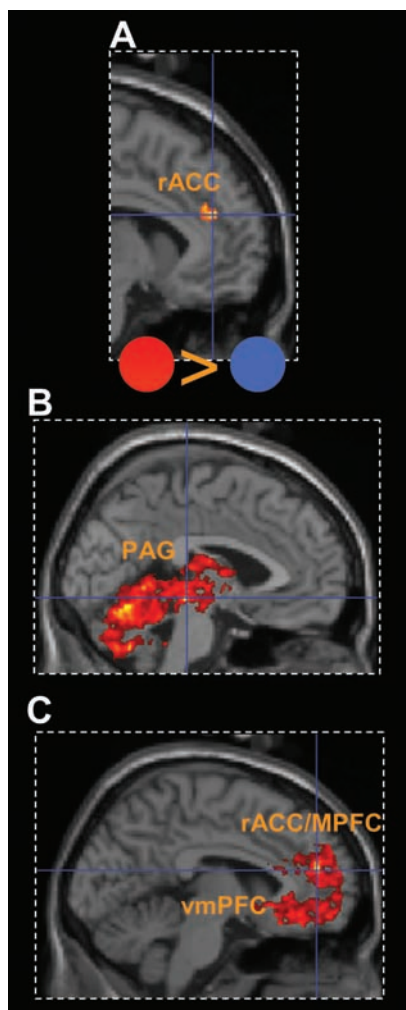


Fig. 2. Statistical parametric maps illustrating BOLD responses to the aversive cues and activation for the $AI_{predator}$ conditions collapsed across blocks. Mean activity is shown for regions within 4 mm of peak. (A and B) Activity for the $AI_{predator}$ (red circle) minus the $AI_{neutral}$ (blue circle) cue in (A) rACC and (B) periaqueductal gray (PAG) activity increased during all $AI_{predator}$ blocks minus yoked blocks. (C) Activity in the rACC/mPFC and vmPFC (table S2) for yoked blocks minus $AI_{predator}$ blocks.

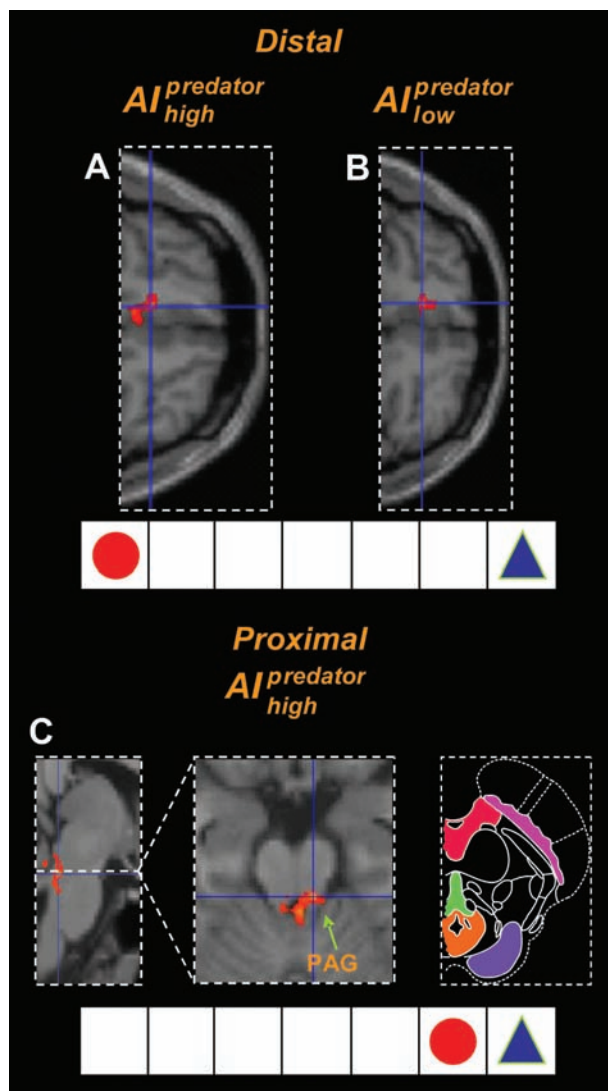


Fig. 3. fMRI results illustrating the imminence effect in the predator condition. For distal threat there was greater activity in vmPFC (horizontal view) for both (A) $AI_{high}^{predator}$ and (B) $AI_{low}^{predator}$ shock expectation. (C) For proximal threat there was greater activity in the PAG for $AI_{high}^{predator}$ [left panel, sagittal view; center panel, horizontal view; right panel, schematic depiction of the midbrain with PAG shown in orange; modified from (27)]. See fig. S2 for images of the PAG activity for the $AI_{low}^{predator}$ imminence. See fig. S4 for coronal view of the PAG activity.

If this forebrain-midbrain threat circuit is mediated by both geographical-temporal and psychological distance, as predicted by theorists (4, 5), we would then expect subject-specific differences in psychological indices of threat to be correlated with PAG activity. We regressed post-scan reports of dread of being chased by the $AI_{\text{predator}}^{\text{high}}$ (9) and confidence of escaping capture with the imminence-driven BOLD signal (Fig. 4). Subjective scores of dread and confidence did not correlate (Pearson $r = -0.016$; $P < 0.96$), which suggests that they tap distinct traits.

Dread of capture correlated with enhanced activity in the PAG (11, -32, -18; $Z = 3.14$), but peaking in the vicinity of the dorsal raphe nuclei (DRN; -1, -26, -19; $Z = 4.65$), for the $AI_{\text{high}}^{\text{predator}}$ condition. A similar pattern was observed for PAG (-5, -32, -18; $Z = 3.33$) and DRN (0, -28, -19; $Z = 4.29$; fig. S5) activity in the $AI_{\text{low}}^{\text{predator}}$ condition (Fig. 4). Decreased dread was associated with medial PFC activity (-3, 48, 24; $Z = 3.56$) for the $AI_{\text{low}}^{\text{predator}}$ condition and ventral PFC activity (3, 38, -17; $Z = 3.37$) for the $AI_{\text{high}}^{\text{predator}}$ condition (table S4). Likewise, decreased confidence of escape was associated with increased activity in the PAG for both the $AI_{\text{high}}^{\text{predator}}$ (2, -29, -19; $Z = 3.19$), and $AI_{\text{low}}^{\text{predator}}$ (-3, -37, -20; $Z = 2.63$) conditions. Increased confidence of escape was associated with increased activity in the vmPFC for both conditions (table S5).

Our results show a dynamic configuration of threat responses that include the PAG and are akin to what might be predicted from animal

models of defensive avoidance (6, 7) and fear (10). When threat was detected, we observed enhanced activity in the rACC and mObfc. The rACC activation encompassed the cytoarchitectonic subdivisions of Brodmann areas 32 and 24c, which have known connections to the amygdala, mObfc, PAG, and brainstem reticular formation; these regions are critical to autonomic, visceromotor, and opioidergic functioning (11). One interpretation is that the rACC activity is associated with the response conflict between fleeing or staying (3), whereas mObfc activity represents the threat value of the AI_{predator} (12). It has been suggested that post-encounter anticipatory anxiety promotes behavior that reduces an aversive state (e.g., avoidance) and may recruit the rACC for this purpose (5, 13). The ACC markedly increases in activity with increased dread of pain (9) and supports our findings of a positive correlation between dread ratings and rACC activity when the $AI_{\text{high}}^{\text{predator}}$ was proximal (table S4). Notably, the ACC produces glutamatergic aversive teaching signals (14) that may regulate avoidance behaviors (15).

As hypothesized, distal threat elicited increased vmPFC activity during the chase phase. It might be argued that this prefrontal activity represents processes where different alternative goal-directed behaviors are compared in order to choose the most effective strategy to avoid the threat or distress (16–18). However, the functions of the vmPFC may also be understood by its connections to the amygdala. The BLA has direct

connections with the vmPFC and mObfc and is important in determining the motivational importance of the stimuli (e.g., the degree of threat), whereas the CeA/BNST of the amygdala are major entryways into the PAG and are important for controlling a repertoire of behavioral and neurovegetative defensive states (3, 5, 17, 19). In this framework, the BLA may be more involved in active responses in the form of guidance or gating of behavior, whereas the CeA/BNST is involved in aversive conditioning and reflexive responding through its descending connections to the PAG (3, 6).

When threat became proximal, we observed increased PAG activity. This forebrain-to-midbrain switch is anatomically credible in light of descending connections between the vmPFC/amygdala and PAG in the primate brain (16, 20, 21). Electrical stimulation of the human PAG can result in heightened fear and anxiety (22). In rats, stimulation of the ventrolateral PAG and dorsolateral PAG promotes passive (e.g., freezing) and active (e.g., escape) coping, respectively (21, 23). The PAG is further divisible along the rostral-caudal axis, implicated in flight and fight (21). Although the functional territories of the human PAG are difficult to dissociate and should be interpreted with caution, our study shows that both the ventral and dorsal portions of the PAG were active during the $AI_{\text{high}}^{\text{predator}}$ condition. Moreover, both the $AI_{\text{high}}^{\text{predator}}$ and the $AI_{\text{low}}^{\text{predator}}$ minus $AI_{\text{low}}^{\text{predator}}$ comparisons were active in the dorsal PAG, supporting the putative role of this region in active avoidance (21).

Activity in the PAG was conspicuously increased during the $AI_{\text{high}}^{\text{predator}}$ condition and for participants with increased dread and decreased confidence of escape. Previous studies have shown that this forebrain-midbrain circuit is abnormal in panic and chronic anxiety patients who show decreased vmPFC but increased gray matter volume and activity in the midbrain encompassing the PAG (24, 25). Intriguingly, the infralimbic vmPFC inhibits stress-induced neural activity in the rodent brainstem and is important in facilitating escape and extinction learning (18, 26). Note also that the vmPFC and mObfc project directly into the dorsolateral PAG (17). Our results therefore support the hypothesis that the PAG is critical during immediate proximal threat, yet may be suppressed or promoted by higher prefrontal regions (16–18).

Our observations concur with the proposition of a hardwired forebrain-midbrain network, which includes the vmPFC at the lowest level of threat and interacts with the midbrain PAG as the threat level increases. From an evolutionary viewpoint, higher cortical systems control behavior when the degree of threat is appraised as non-life-endangering and guides the organism to choose the most effective and resourceful strategy for instrumental avoidance. At extreme levels of threat, the PAG may in turn inhibit more complex control processes when a fast and indeed obligatory response is required, preparing the organism for survival and possible tissue

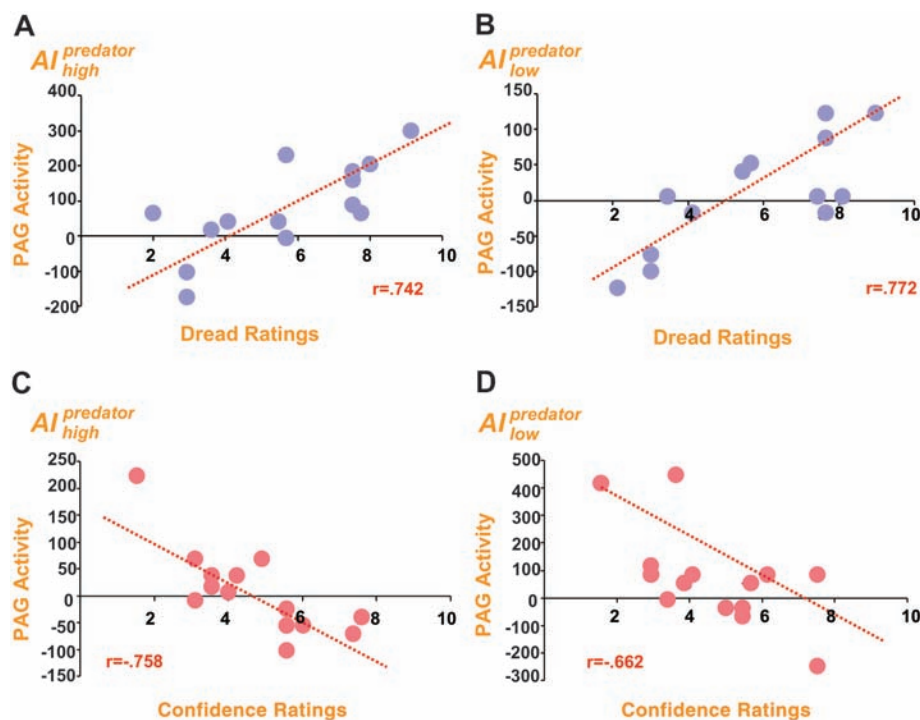


Fig. 4. Subject-specific differences in dread of capture and confidence of escape. (A and B) Scatterplots of regions of the PAG that correlated with threat distance and increased dread of being caught by the (A) $AI_{\text{high}}^{\text{predator}}$ and (B) $AI_{\text{low}}^{\text{predator}}$. (C and D) Regions associated with threat distance and decreased confidence of escaping the (C) $AI_{\text{high}}^{\text{predator}}$ and (D) $AI_{\text{low}}^{\text{predator}}$. Each point represents an individual's response on post-scan questionnaire.

damage (3, 16–18, 21). Understanding the balance between forebrain and midbrain responses to threat might illuminate the pathophysiology of neuropsychiatric disturbances, including chronic anxiety and panic disorder, where brainstem involvement has long been suspected.

References and Notes

- R. J. Blanchard, D. C. Blanchard, in *Fear and Defence*, P. F. Brain, R. J. Blanchard, S. Parmigiani, Eds. (Harwood Academic, London, 1990), pp. 89–108.
- M. S. Fanselow, L. S. Lester, in *Evolution and Learning*, R. C. Bolles, M. D. Beecher, Eds. (Erlbaum, Hillsdale, NJ, 1988), pp. 185–211.
- M. S. Fanselow, *Psychon. Bull. Rev.* **1**, 429 (1994).
- M. G. Craske, *Anxiety Disorders: Psychological Approaches to Theory and Treatment* (Westview, Boulder, CO, 1999).
- V. Rau, M. S. Fanselow, in *Understanding Trauma: Integrating Biological, Clinical, and Cultural Perspectives* L. J. Kirmayer, R. Lemelson, M. Barad, Eds. (Cambridge Univ. Press, New York, 2007), pp. 27–40.
- N. McNaughton, P. J. Corr, *Neurosci. Biobehav. Rev.* **28**, 285 (2004).

- J. F. W. Deakin, F. G. Graeff, *J. Psychopharmacol.* **5**, 305 (1991).
- P. J. Lang, M. Davis, *Prog. Brain Res.* **156**, 3 (2006).
- G. S. Berns *et al.*, *Science* **312**, 754 (2006).
- J. M. Gorman, J. M. Kent, G. M. Sullivan, J. D. Coplan, *Am. J. Psychiatry* **157**, 493 (2000).
- O. Devinsky, M. J. Morrell, B. A. Vogt, *Brain* **118**, 279 (1995).
- P. H. Rudebeck, M. J. Buckley, M. E. Walton, M. F. Rushworth, *Science* **313**, 1310 (2006).
- J. C. Hsieh, S. Stone-Elander, M. Ingvar, *Neurosci. Lett.* **262**, 61 (1999).
- J. P. Johansen, H. L. Fields, *Nat. Neurosci.* **7**, 398 (2004).
- K. Shima, J. Tanji, *Science* **282**, 1335 (1998).
- G. Hadjipavlou, P. Dunckley, T. E. Behrens, I. Tracey, *Pain* **123**, 169 (2006).
- J. L. Price, *J. Comp. Neurol.* **493**, 132 (2005).
- J. Amat *et al.*, *Nat. Neurosci.* **8**, 365 (2005).
- F. G. Graeff, *Neurosci. Biobehav. Rev.* **28**, 239 (2004).
- N. S. Floyd, J. L. Price, A. T. Ferry, K. A. Keay, R. Bandler, *J. Comp. Neurol.* **422**, 556 (2000).
- R. Bandler, K. A. Keay, N. Floyd, J. Price, *Brain Res. Bull.* **53**, 95 (2000).

- B. S. Nashold, W. P. Wilson, D. G. Slaughter, *J. Neurosurg.* **30**, 14 (1969).
- M. R. Vianna *et al.*, *Braz. J. Med. Biol. Res.* **34**, 233 (2001).
- X. Protopopescu *et al.*, *Neuroreport* **17**, 361 (2006).
- E. M. Reiman *et al.*, *Arch. Gen. Psychiatry* **46**, 493 (1989).
- E. A. Phelps, M. R. Delgado, K. I. Nearing, J. E. LeDoux, *Neuron* **43**, 897 (2004).
- H. M. Duvernoy, *The Human Brain Stem and Cerebellum* (Springer, New York, 1995).
- We thank C. Hagan and U. Frith for helpful comments. Supported by a Brain Research Trust Prize studentship (D.M.) and by the Wellcome Trust.

Supporting Online Material

www.sciencemag.org/cgi/content/full/317/5841/1079/DC1
Materials and Methods
Figs. S1 to S5
Tables S1 to S5
References

26 April 2007; accepted 10 July 2007
10.1126/science.1144298

Astrocytes Potentiate Transmitter Release at Single Hippocampal Synapses

Gertrudis Perea and Alfonso Araque*

Astrocytes play active roles in brain physiology. They respond to neurotransmitters and modulate neuronal excitability and synaptic function. However, the influence of astrocytes on synaptic transmission and plasticity at the single synapse level is unknown. Ca^{2+} elevation in astrocytes transiently increased the probability of transmitter release at hippocampal area CA3-CA1 synapses, without affecting the amplitude of synaptic events. This form of short-term plasticity was due to the release of glutamate from astrocytes, a process that depended on Ca^{2+} and soluble *N*-ethylmaleimide-sensitive factor attachment protein receptor (SNARE) protein and that activated metabotropic glutamate receptors (mGluRs). The transient potentiation of transmitter release became persistent when the astrocytic signal was temporally coincident with postsynaptic depolarization. This persistent plasticity was mGluR-mediated but *N*-methyl-D-aspartate receptor-independent. These results indicate that astrocytes are actively involved in the transfer and storage of synaptic information.

Recent data have demonstrated the existence of bidirectional communication between astrocytes and neurons (1). In addition to responding to synaptic activity, astrocytes release gliotransmitters (2), which modulate neuronal excitability and neurotransmission (3). To investigate the consequences of astrocyte Ca^{2+} elevations on evoked synaptic transmission at single hippocampal synapses, we performed paired recordings from CA1 pyramidal neurons and single astrocytes (4). Astrocytes were loaded with the Ca^{2+} -cage *o*-nitrophenyl-EGTA (NP-EGTA) to be selectively stimulated by ultraviolet (UV)-flash photolysis, while we stimulated Schaffer collaterals using the minimal stimulation meth-

od that activates single, or very few synapses (5, 6).

First, we established that single synapses were stimulated in our experimental model by quantifying the synaptic transmission properties of the excitatory postsynaptic currents (EPSCs) (Fig. 1). Synaptic responses showed failures and successes in neurotransmitter release [probability of release (Pr) was 0.34 ± 0.02 ; range, 0.13 to 0.54; $n = 34$]; regular amplitude of successful responses (termed “synaptic potency”; 20.9 ± 1.3 pA; range, 8.5 to 37.5 pA; $n = 34$); and relatively low synaptic efficacy [i.e., the mean amplitude of all responses including failures: 6.9 ± 0.5 pA [range, 2.8 to 10.2 pA; $n = 34$ (fig. S1)]]. Paired-pulse stimulation facilitated the second EPSC relative to the first EPSC [paired-pulse facilitation (PPF) index was 0.48 ± 0.05 ; $n = 20$ (fig. S1)]. To stimulate astrocytes, we patch-clamped single passive astrocytes located

in the stratum radiatum near (<50 μm from) the stimulating pipette. We included NP-EGTA and fluo-4 in the recording pipette to selectively activate single astrocytes and to monitor their Ca^{2+} levels, respectively (Fig. 1A). UV-flash trains evoked astrocyte Ca^{2+} elevations that were reliably repeated by successive stimuli [15 out of 15 astrocytes (fig. S2)].

After the control recording of EPSCs, NP-EGTA-loaded astrocytes were photo-stimulated. In 18 out of 38 neuron-astrocyte pairs [47% (Fig. 1D)] astrocytic Ca^{2+} elevations transiently (~ 2 min) increased the synaptic efficacy (from 4.8 ± 0.6 pA to 6.2 ± 1.0 pA; $n = 18$; $P < 0.05$). This was due to a transient enhancement of Pr rather than a postsynaptic modulation (Fig. 1, F and G). Indeed, although Pr increased after astrocyte stimulation (from 0.24 ± 0.03 to 0.33 ± 0.04 ; $n = 18$; $P < 0.001$), the synaptic potency was unchanged (from 15.2 ± 1.3 pA to 15.7 ± 1.9 pA; $n = 18$; $P = 0.96$). Moreover, the PPF index changed from 0.64 ± 0.06 to 0.33 ± 0.10 after astrocyte stimulation [(fig. S3) $n = 18$; $P < 0.01$], which is consistent with a presynaptic mechanism of action. Furthermore, the kinetic properties of EPSCs were unaffected (respective rise and decay time constants before and after astrocyte stimulation were $\tau_{\text{on}} = 1.48 \pm 0.22$ ms and 1.45 ± 0.23 ms; $P = 0.34$; $\tau_{\text{off}} = 9.80 \pm 0.94$ ms and 10.31 ± 1.77 ms; $P = 0.43$; $n = 6$). These effects were reliably evoked by successive astrocyte stimulation (Fig. 2A).

In the absence of NP-EGTA or with the NP-EGTA-filled pipette placed outside the cell, UV flashes did not modify synaptic transmission (fig. S4), which indicated that the effects were not due to photo-stimulation of synaptic terminals and that Ca^{2+} elevation in astrocytes is necessary and sufficient to potentiate the synaptic transmission.

We further analyzed whether the astrocyte-induced neuromodulation could also be evoked by stimuli that elevate astrocyte Ca^{2+} through transmitter receptor activation. We used adeno-

Instituto Cajal, Consejo Superior de Investigaciones Científicas, Madrid, Spain.

*To whom correspondence should be addressed. E-mail: araque@cajal.csic.es